

# Superconductivity from Repulsive Interactions in Rhombohedral Trilayer Graphene: a Kohn-Luttinger-Like Mechanism

Tommaso Cea and Pierre A. Pantaleón  
*Imdea Nanoscience, Faraday 9, 28015 Madrid, Spain*

Võ Tiến Phong  
*Department of Physics and Astronomy, University of Pennsylvania, Philadelphia PA 19104*

Francisco Guinea  
*Imdea Nanoscience, Faraday 9, 28015 Madrid, Spain*  
*Donostia International Physics Center, Paseo Manuel de Lardizábal 4, 20018 San Sebastián, Spain and*  
*Ikerbasque. Basque Foundation for Science. 48009 Bilbao. Spain.*  
 (Dated: September 10, 2021)

We study the emergence of superconductivity in rhombohedral trilayer graphene due purely to the long-range Coulomb repulsion. This repulsive-interaction-driven phase in rhombohedral trilayer graphene is significantly different from those found in twisted bilayer and trilayer graphenes. In the latter case, the nontrivial momentum-space geometry of the Bloch wavefunctions leads to an effective attractive electron-electron interaction; this allows for less modulated order parameters and for spin-singlet pairing. In rhombohedral trilayer graphene, we instead find spin-triplet superconductivity with critical temperatures up to 0.15 K. The critical temperatures strongly depend on electron filling and peak where the density of states diverge. The order parameter shows a significant modulation within each valley pocket of the Fermi surface.

*Introduction* – Recently, superconductivity was experimentally observed in a three-layer graphene stack with rhombohedral (ABC) arrangement that is tunable by an applied interlayer bias [1]. Following this, several theories have been proposed to account for the onset of effective attractive interaction between electrons mediated by different pairing mechanisms: electron-phonon coupling [2], spin fluctuations near an antiferromagnetic phase [3, 4], direct coupling by the screened Coulomb interaction [5], or pairing mediated by the proximity to a correlated insulator [4, 6]. Although different in details, all of these proposals made use of the fact that the density of states (DOS) of ABC trilayer graphene near charge neutrality can be greatly enhanced by applying a gate voltage across the three layers. Ignoring possible weak spin-orbit couplings, intrinsic ABC trilayer graphene is a semimetal with an approximate cubic band degeneracy at the zone corners [7–24]. When resolved close to these points, the cubic degeneracy actually splits into three Dirac cones, creating a trigonally-warped Fermi surface. As a perpendicular electric field is applied, inversion symmetry is broken, and these Dirac points acquire a finite mass. As a result, the local band dispersion can be nearly quenched, generating a van Hove singularity that favors the emergence of correlated electronic phases.

Similar physics can also be found in three-dimensional (3D) rhombohedral graphite, which is a nodal line semimetal that has a flat electronic band at the top and bottom surfaces of a sufficiently wide stack [25]. The associated divergent DOS is expected to enhance electron-electron interactions and lead to broken-symmetry phases, including superconductivity [13, 14]

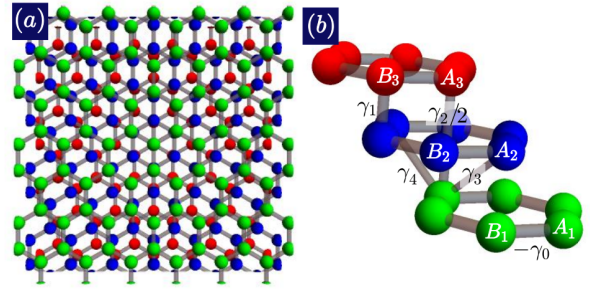


Figure 1. **Lattice structure of ABC RTG.** (a) The 3D crystal structure viewed from the top. (b) Some representative hopping parameters between carbon atoms.

and magnetism [16]. Experimentally, gaps and broken-symmetry phases in finite rhombohedral stacks have been reported [15, 17–19, 21–24]. The partially flat bands in rhombohedral stacks make these systems spectrally similar to magic-angle twisted bilayer graphene [26, 27], importantly without the need for a superlattice structure.

Inspired by these observations, we analyze here the appearance of superconductivity in rhombohedral trilayer graphene (RTG). We assume that the only electron-electron coupling is via the long-range Coulomb interaction. We analyze the possibility of pairing using a diagrammatic technique, similar to the Kohn-Luttinger approach [28] to superconductivity due to repulsive interactions (see also [5]). The same scheme has been already applied to twisted bilayer graphene [29], and to twisted trilayer graphene [30]. The use of the same technique allows us to compare the emergence of superconductivity in twisted and rhombohedral stacks. As discussed below,

the calculation leads to superconducting (SC) phases in both types of materials, although the physical origin of superconductivity and the superconducting order parameter (OP) are significantly different in the two cases.

*Tight-binding Hamiltonian* – The 3D crystal structure

$$H_{tb}(\mathbf{k}) = \begin{pmatrix} \Delta_1 + \Delta_2 & -\gamma_0 u(\mathbf{k}) & \gamma_4 u^*(\mathbf{k}) & \gamma_1 & 0 & 0 \\ -\gamma_0 u^*(\mathbf{k}) & \Delta_1 + \Delta_2 + \delta & \gamma_3 v(\mathbf{k}) & \gamma_4 u^*(\mathbf{k}) & \gamma_2/2 & 0 \\ \gamma_4 u(\mathbf{k}) & \gamma_3 v^*(\mathbf{k}) & -2\Delta_2 & -\gamma_0 u(\mathbf{k}) & \gamma_4 v^*(\mathbf{k}) & \gamma_1 \\ \gamma_1 & \gamma_4 u(\mathbf{k}) & -\gamma_0 u^*(\mathbf{k}) & -2\Delta_2 & \gamma_3 u(\mathbf{k}) & \gamma_4 u^*(\mathbf{k}) \\ 0 & \gamma_2/2 & \gamma_4 v(\mathbf{k}) & \gamma_3 u^*(\mathbf{k}) & \Delta_2 - \Delta_1 + \delta & -\gamma_0 v(\mathbf{k}) \\ 0 & 0 & \gamma_1 & \gamma_4 u(\mathbf{k}) & -\gamma_0 v^*(\mathbf{k}) & \Delta_2 - \Delta_1 \end{pmatrix}, \quad (1)$$

$\gamma_0$	$\gamma_1$	$\gamma_2$	$\gamma_3$	$\gamma_4$	$\delta$	$\Delta_2$
3.1	0.38	-0.015	0.29	0.141	-0.0105	-0.0023

Table I. Minimal tight-binding parameters of RTG, expressed in eV (see also [24, 32]).

where  $\gamma_i$  are the hopping amplitudes,  $\Delta_1$  is a potential difference between nearest neighbor layers which takes into account an external displacement field,  $\Delta_2$  is the potential difference between the middle layer compared to mean potential of the outer layers,  $\delta$  encodes an on-site potential which is only present at sites  $B_1$  and  $A_3$  since these two atoms do not have a neighbor on the middle layer, and  $u(\mathbf{k}) = 1 + 2 \cos(k_x a/2) e^{-ik_y a\sqrt{3}/2}$ ,  $v(\mathbf{k}) = e^{ik_y a\sqrt{3}} u(\mathbf{k})$ , with  $a = 2.46 \text{ \AA}$  is the lattice constant of graphene. The optimal values of the minimal tight-binding parameters,  $\gamma_i$  and  $\delta$ , have been reported in the literature [11, 19, 20, 31–33]. Here we use the ones calculated in Refs. [24, 32]. These parameters are tabulated in Table I.

The single-particle band structure corresponding to model (1) for  $\Delta_1 = 50 \text{ meV}$  along a high-symmetry path of the Brillouin zone (BZ) is shown in Fig. 2(a). Since we are only interested in the lightly-doped regime, only the local band structure around  $E = 0$  is of relevance to us. This region in momentum space is shown in Fig. 2(b) along with the corresponding DOS expressed in units of  $\text{eV}^{-1} A_c^{-1}$ , where  $A_c = \sqrt{3}a^2/2$  is the area of one unit cell. We draw attention to the sizeable gap at the charge neutrality point (CNP) generated by the external electric field, and to the van Hove singularities at the gap's edges due to band flattening at  $K$  and  $K'$ . See the Supplementary Information for more details on the non interacting band structure.

*Long-range Coulomb interaction and internal screening* – To account for electron-electron interactions, we assume that two electrons separated by a distance  $r$  ex-

perience a  $r^{-2}$  long-range Coulomb repulsion

$$V_C(r) = \begin{cases} \frac{e^2}{4\pi\epsilon_0\epsilon r} & , \text{ for } r \neq 0, \\ \frac{w_0}{\epsilon} & , \end{cases} \quad (2)$$

where  $e$  is the electron charge,  $\epsilon_0$  is the dielectric constant of vacuum, and  $\epsilon$  is the relative dielectric constant of the environment. In this work, we set  $\epsilon = 4$ , which reproduces accurately the screening by a substrate of hexagonal boron nitride (hBN). The parameter  $w_0$  accounts for the local repulsion, which we set to  $w_0 = 17 \text{ eV}$  following Ref. [34]. As the potential  $V_C$  varies slowly on the atomic scale, we approximate the interaction between two electrons as only depending on the distance between the centers of the two unit cells in which the electrons reside. In reciprocal space,  $V_C$  is given by:

$$V_C(\mathbf{q}) = \sum_{\mathbf{R}} V_C(|\mathbf{R}|) e^{-i\mathbf{q}\cdot\mathbf{R}}, \quad (3)$$

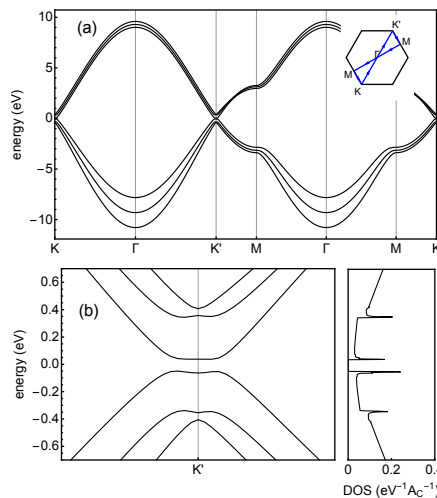


Figure 2. **Band structure of RTG.** (a) Full band structure calculated for  $\Delta_1 = 50 \text{ meV}$ . The inset shows the BZ and the high-symmetry path used for calculation. (b) Left: detail of the band structure close to  $K'$ . (b) Right: DOS.

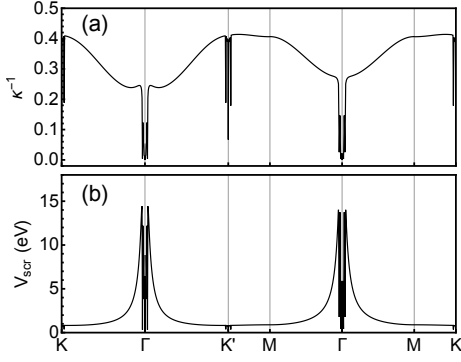


Figure 3. **Screened Coulomb potential.** (a) Inverse of the dielectric function,  $\kappa^{-1}(\mathbf{q}) = [1 - V_C(\mathbf{q})\Pi(\mathbf{q})]^{-1}$ . (b) Screened potential,  $V_{scr}(\mathbf{q})$ . The profiles are computed along the high-symmetry path shown in Fig. 2(a), and obtained for  $\Delta_1 = 50$  meV and electronic density  $n_e = -1.91 \times 10^{12}$  cm $^{-2}$ .

where  $\mathbf{q} \in \text{BZ}$ , the sum runs over all positions  $\mathbf{R}$  of the lattice, with periodic boundary condition imposed by the finite grid used to sample the BZ.

In order to describe internal screening due to particle-hole excitations, we use the static random phase approximation (RPA), leading to the usual renormalization of  $V_C$

$$V_{scr}(\mathbf{q}) = \frac{V_C(\mathbf{q})}{1 - V_C(\mathbf{q})\Pi(\mathbf{q})}, \quad (4)$$

where  $\Pi(\mathbf{q})$  is the zero-frequency limit of the charge susceptibility, as given by

$$\Pi(\mathbf{q}) = \frac{2}{N_c} \sum_{\mathbf{k}n\mathbf{m}} \frac{f(\xi_{n,\mathbf{k}}) - f(\xi_{m,\mathbf{k}+\mathbf{q}})}{\epsilon_{n,\mathbf{k}} - \epsilon_{m,\mathbf{k}+\mathbf{q}}} \times \quad (5)$$

$$\times |\langle \psi_{m,\mathbf{k}+\mathbf{q}} | \psi_{n,\mathbf{k}} \rangle|^2,$$

where  $N_c$  is the number of unit cells,  $\epsilon_{n,\mathbf{k}}$  is the  $n$ -th band energy at wavevector  $\mathbf{k}$ ,  $\psi_{n,\mathbf{k}}$  is the corresponding six-component eigenvector,  $f(\xi) = [1 + e^{\xi/(K_B T)}]^{-1}$  is the Fermi-Dirac distribution at the temperature  $T$ ,  $\xi_{n,\mathbf{k}} = \epsilon_{n,\mathbf{k}} - \mu$ , and  $\mu$  is the chemical potential. The factor of two in front of Eq. (5) accounts for spin degeneracy. As an example, Fig. 3 shows (a) the profile of the inverse of the dielectric function,  $\kappa^{-1}(\mathbf{q}) = [1 - V_C(\mathbf{q})\Pi(\mathbf{q})]^{-1}$ , and (b) of the screened potential,  $V_{scr}(\mathbf{q})$ , computed along the high-symmetry path of the BZ shown in Fig. 2(a), and obtained for  $\Delta_1 = 50$  meV and electronic density  $n_e = -1.91 \times 10^{12}$  cm $^{-2}$ . To perform the calculation, we used  $N_c = 12 \times 10^4$ , which is enough to finely resolve the band structure close to the Fermi surface (FS). The results display an overall strong screening. Remarkably,  $V_{scr}(\mathbf{q})$  vanishes at the centre of the BZ, the point  $\Gamma$ , which means that  $\Pi(\mathbf{q})$  diverges as  $\mathbf{q} \rightarrow 0$  and implies that  $V_{scr}$  is locally attractive in real space.

*Superconductivity* – Next, we assume that the interaction which leads to pairing in RTG is the long-range Coulomb interaction (Ref. [5] makes the same assumption). The calculations carried out in Ref. [29, 30] include, for completeness, the coupling of electronic charge oscillations to longitudinal phonons, as these phonons modify the screening of the Coulomb interaction. It is interesting to note that the inclusion of longitudinal phonons does not change significantly the results reported here.

The critical temperature for the onset of superconductivity in RTG can be obtained from the linearized gap equation

$$\Delta_{ij}(\mathbf{k}) = -\frac{K_B T}{N_c} \sum_{\mathbf{k}'\omega} \sum_{i'j'} V_{scr}(\mathbf{k} - \mathbf{k}') \times \quad (6)$$

$$\times G_{ii'}(\mathbf{k}', i\hbar\omega) G_{jj'}(-\mathbf{k}', -i\hbar\omega) \Delta_{i'j'}(\mathbf{k}'),$$

where  $\omega$  are fermionic Matsubara frequencies,  $i, i', j, j'$  label the sub-lattice/layer degree of freedom, and  $G_{ii'}(\mathbf{k}, i\hbar\omega)$  is the normal-state single-particle Green's function

$$G_{ii'}(\mathbf{k}, i\hbar\omega) = \sum_n \frac{\psi_{n,\mathbf{k}}^i \psi_{n,\mathbf{k}}^{i'*}}{i\hbar\omega - \xi_{n,\mathbf{k}}}. \quad (7)$$

Our framework is similar to the Kohn-Luttinger scheme [28]. The approach in [28] includes all processes up to second order in perturbation theory. Our approach neglects exchange-like diagrams, but, on the other hand, includes all bubble diagrams to infinite orders. The multiplicity of these diagrams is equal to the number of electron flavors, in the present case  $\mathcal{N}_f = 2$ . Hence, it can be considered an expansion in powers of  $\mathcal{N}_f^{-1}$ .

Upon projecting Eq. (6) onto the band basis and performing the Matsubara sum, we rewrite it as

$$\Delta_{m_1 m_2}(\mathbf{k}) = \sum_{\mathbf{k}' n_1 n_2} \Gamma_{m_1 m_2, n_1 n_2}(\mathbf{k}, \mathbf{k}') \Delta_{n_1 n_2}(\mathbf{k}'), \quad (8)$$

where

$$\Delta_{m_1 m_2}(\mathbf{k}) = \sum_{ij} \psi_{m_1, \mathbf{k}}^{i,*} \psi_{m_2, \mathbf{k}}^i \Delta_{ij}(\mathbf{k}) \times \quad (9)$$

$$\times \sqrt{\frac{f(-\xi_{m_2, \mathbf{k}}) - f(\xi_{m_1, \mathbf{k}})}{\xi_{m_2, \mathbf{k}} + \xi_{m_1, \mathbf{k}}}},$$

and  $\Gamma_{m_1 m_2, n_1 n_2}(\mathbf{k}, \mathbf{k}')$  is the Hermitian kernel

$$\Gamma_{m_1 m_2, n_1 n_2}(\mathbf{k}, \mathbf{k}') = -\frac{1}{N_c} V_{scr}(\mathbf{k} - \mathbf{k}') \langle \psi_{m_1, \mathbf{k}} | \psi_{n_1, \mathbf{k}'} \rangle \langle \psi_{n_2, \mathbf{k}'} | \psi_{m_2, \mathbf{k}} \rangle \times \quad (10)$$

$$\times \sqrt{\frac{f(-\xi_{m_2, \mathbf{k}}) - f(\xi_{m_1, \mathbf{k}})}{\xi_{m_2, \mathbf{k}} + \xi_{m_1, \mathbf{k}}}} \sqrt{\frac{f(-\xi_{n_2, \mathbf{k}'}) - f(\xi_{n_1, \mathbf{k}'})}{\xi_{n_2, \mathbf{k}'} + \xi_{n_1, \mathbf{k}'}}}.$$

We make use of the time-reversal symmetry of Hamiltonian (1), which implies  $\xi_{n, -\mathbf{k}} = \xi_{n, \mathbf{k}}$  and  $\psi_{m, -\mathbf{k}} = \psi_{m, \mathbf{k}}^*$ . At a critical temperature,  $T_c$ , the largest eigenvalue of the

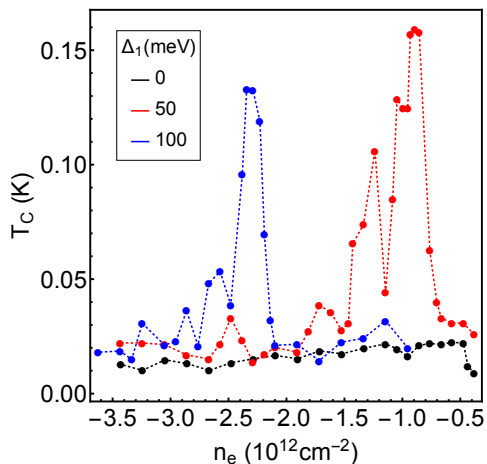


Figure 4. **Critical temperature as a function of filling for various values of the interlayer bias.**

kernel  $\Gamma_{m_1 m_2, n_1 n_2}(\mathbf{k}, \mathbf{k}')$  is 1. The corresponding eigenvector provides the symmetry of the OP.

We diagonalize numerically the Kernel of Eq. (10). As the leading contribution to Eq. (8) comes from the states closest to the FS, we cut off phase space by considering only the states satisfying  $|\xi_{n, \mathbf{k}}| \leq w$ , with  $w = 30$  meV. In order to rule out finite-size effects and to finely sample the FS at densities on the order of  $\sim 10^{12}$  cm $^{-2}$ , we implement a length renormalization:  $a \rightarrow a_s = s \times a$ , where  $s > 1$  is the scale factor and  $a_s$  is the effective lattice spacing. This procedure defines an effective tight-binding model where the hopping amplitudes  $\gamma_0$ ,  $\gamma_3$ , and  $\gamma_4$  are rescaled according to  $\gamma_i \rightarrow \gamma_{i, s} = \gamma_i / s$ ,  $i = 0, 3, 4$ . This procedure reduces the size of the BZ by a factor of  $s^2$ , allowing us to study considerably larger meshes that would otherwise be numerically prohibitive. In doing so, we are able to obtain a finer momentum resolution close to the CNP to improve accuracy.

*Critical superconducting temperature* – Fig. 4 shows the value of the critical temperature as a function of electronic density,  $n_e$ , for  $\Delta_1 = 0, 50, 100$  meV. The results are obtained with a grid of  $3 \times 10^4$  points in the BZ, upon rescaling with  $s = 10$ , meaning that we are considering  $3 \times 10^6$  unit cells of the atomic RTG. The critical temperatures feature pronounced maxima on the order of 0.1 – 0.2 K for finite values of  $\Delta_1$ . In contrast, we do not observe any appreciable enhancement of  $T_c$  without a bias. To gain insight into this behavior, we show in Fig. 5 the bands (a) and DOS (b) close to the CNP, obtained for the values of  $\Delta_1$  considered in Fig. 4. We observe that a finite bias significantly enhances the van Hove singularities near the band edge, a feature that is absent in the zero-bias limit. In Fig. 5, the horizontal dashed lines identify the Fermi levels corresponding to the values of  $n_e$  which maximize  $T_c$  in Fig. 4. These Fermi energies match the position of the Van Hove singularities with great accuracy, showing that superconductivity

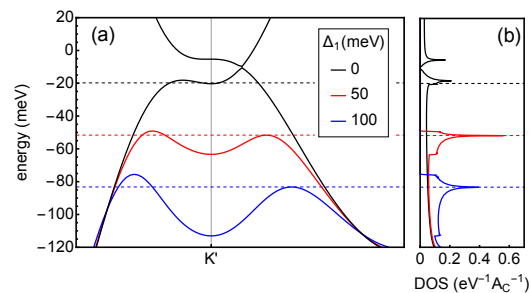


Figure 5. **Bias-induced van Hove singularities.** Electronic bands (a) and DOS (b) close to the CNP, obtained for the values of  $\Delta_1$  considered in Fig. 4. The horizontal dashed lines identify the Fermi levels corresponding to the values of  $n_e$  which maximize  $T_c$  in Fig. 4.

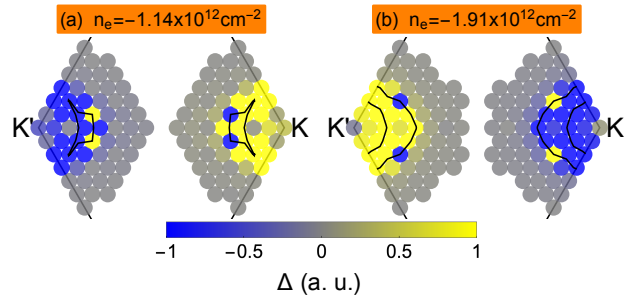


Figure 6. **Symmetry of the superconducting order parameter in the vicinity of  $K$  and  $K'$ .** These are calculated for  $\Delta_1 = 50$  meV and  $n_e = -1.14 \times 10^{12}$  cm $^{-2}$  (a) and  $-1.91 \times 10^{12}$  cm $^{-2}$  (b). The black lines identify the FS.

is strongly enhanced when the Fermi level is close to a peak in the DOS. In addition, given a finite bias, a sizeable  $T_c$  survives only in a narrow region of  $n_e$  around an optimal value, thus providing a tool to trigger superconductivity by tuning  $n_e$  and/or  $\Delta_1$ . It is worth noting that the results reported in Fig. 4 are in reasonable agreement with the experimental data of Ref. [1], in terms of both the magnitude of the critical temperatures and the range of densities reported.

*Symmetry of the superconducting order parameter* – Finally, we study the superconducting order parameter. Fig. 6 shows the symmetry of the SC OP in the vicinity of  $K$  and  $K'$ , obtained for  $\Delta_1 = 50$  meV and  $n_e = -1.14, -1.91 \times 10^{12}$  cm $^{-2}$ , which are representative of most of the cases we have studied. The black lines identify the FS. These results have been obtained without scaling,  $s = 1$ , by using  $N_c = 12 \times 10^4$  unit cells of the atomic RTG. As expected, the OP is nonzero only in a narrow region of the BZ around the FS, implying that only the electrons close to the Fermi level participate in Cooper pairing. In addition, the OP clearly displays  $A_2$  symmetry, meaning that it is antisymmetric upon exchanging  $\mathbf{k} \rightarrow -\mathbf{k}$ . Because Hamiltonian (1) is spin degenerate and the interaction, Eq. (2), does

not couple different spin flavors, the gap equations (6) and (8) do not contain explicitly the spin indices, implying that they cannot distinguish between spin-triplet and spin-singlet superconductivity. However,  $A_2$  symmetry necessarily implies that the Cooper pairs must be symmetric (i. e. triplet) in spin space in order for the total wavefunction to be antisymmetric upon exchanging the two electrons[35]. Finally, it is worth noting that the OP changes sign within each valley pocket of the FS. The pairing potential represented by the kernel  $\Gamma_{m_1 m_2, n_1 n_2}(\mathbf{k}, \mathbf{k}')$ , Eq. (10), is repulsive in reciprocal space, and the eigenvector corresponding to the eigenvalue 1 cannot have a constant sign. This is a general feature of weak-coupling superconductivity induced by electronic interactions, where the superconducting wave function displays a high angular momentum, as is the case for  $p$ - or  $f$ -wave superconductivity.

*Conclusions* – We have analyzed diagrammatically the existence of superconductivity in RTG. We assume that the leading electron-electron interaction is Coulomb repulsion. Our results show that this interaction is enough to induce superconductivity in RTG, although it cannot be excluded that other excitations can contribute [2–4, 6]. The large DOS in RTG at low fillings leads to a significant screening of the interaction. The screened Coulomb repulsion induces superconductivity with critical temperatures upward 0.15 K that depend strongly on electron filling and are correlated with peaks in the DOS. The OP fluctuates in sign within each valley, in agreement with the existence of a repulsive interaction at small momenta. Overall, the OP is antisymmetric in the BZ, so that the pairs must be spin triplets. The method used here has also been applied to the study of superconductivity in twisted bilayer and trilayer graphene [29, 30]. In those cases, however, the combination of Umklapp processes and the complexity of the wavefunctions turns the interaction attractive at small momenta. As a result, the OP does not change within individual pockets of the FS. The superconductivity can be spin singlet/valley triplet or spin triplet/valley singlet. The small momentum modulation of the OP implies that long-range disorder is pair breaking in RTG, while that is not the case in twisted bilayer/trilayer graphene.

*Acknowledgements.* This work was supported by funding from the European Commission, under the Graphene Flagship, Core 3, grant number 881603, and by the grants NMAT2D (Comunidad de Madrid, Spain), SprQuMat and SEV-2016-0686, (Ministerio de Ciencia e Innovación, Spain). VTP acknowledges support from the NSF Graduate Research Fellowships Program and the P.D. Soros Fellowship for New Americans.

- 
- [1] H. Zhou, T. Xie, T. Taniguchi, K. Watanabe, and A. F. Young, Superconductivity in rhombohedral trilayer graphene, *Nature* (2021).
  - [2] Y.-Z. Chou, F. Wu, J. D. Sau, and S. Das Sarma, Acoustic-phonon-mediated superconductivity in rhombohedral trilayer graphene, arXiv e-prints , arXiv:2106.13231 (2021), [arXiv:2106.13231 \[cond-mat.supr-con\]](#).
  - [3] H. Dai, J. Hou, X. Zhang, Y. Liang, and T. Ma, Mott insulating state and d + i d superconductivity in an ABC graphene trilayer, *Phys. Rev. B* **104**, 035104 (2021), [arXiv:2009.14647 \[cond-mat.str-el\]](#).
  - [4] Z. Dong and L. Levitov, Superconductivity in the vicinity of an isospin-polarized state in a cubic Dirac band, arXiv e-prints , arXiv:2109.01133 (2021), [arXiv:2109.01133 \[cond-mat.supr-con\]](#).
  - [5] A. Ghazaryan, T. Holder, S. Maksym, and E. Berg, Unconventional superconductivity in systems with annular fermi surfaces: Application to rhombohedral trilayer graphene, (2021).
  - [6] S. Chatterjee, T. Wang, E. Berg, and M. P. Zaletel, Inter-valley coherent order and isospin fluctuation mediated superconductivity in rhombohedral trilayer graphene, (2021), [arXiv:2109.00002](#).
  - [7] J. W. McClure, Electron energy band structure and electronic properties of rhombohedral graphite, *Carbon* **7**, 425 (1969).
  - [8] M. S. Dresselhaus and G. Dresselhaus, Intercalation compounds of graphite, *Adv. in Phys.* **51**, 1 (2002).
  - [9] D. P. Arovas and F. Guinea, Stacking faults, bound states, and quantum hall plateaus in crystalline graphite, *Phys. Rev. B* **78**, 245416 (2008).
  - [10] F. Zhang, B. Sahu, H. Min, and A. H. MacDonald, Band structure of *abc*-stacked graphene trilayers, *Phys. Rev. B* **82**, 035409 (2010).
  - [11] M. Koshino, Interlayer screening effect in graphene multilayers with *aba* and *abc* stacking, *Phys. Rev. B* **81**, 125304 (2010).
  - [12] W. Bao, L. Jing, J. Velasco Jr., Y. Lee, D. Liu, G. and Tran, B. Standley, M. Aykol, S. B. Cronin, D. Smirnov, M. Koshino, E. McCann, M. Bockrath, and C. N. Lau, Stacking-dependent band gap and quantum transport in trilayer graphene, *Nature Phys.* **7**, 948 (2011).
  - [13] N. B. Kopnin, T. T. Heikkilä, and G. E. Volovik, High-temperature surface superconductivity in topological flat-band systems, *Phys. Rev. B* **83**, 220503 (2011).
  - [14] N. B. Kopnin, M. Ijäs, A. Harju, and T. T. Heikkilä, High-temperature surface superconductivity in rhombohedral graphite, *Phys. Rev. B* **87**, 140503 (2013).
  - [15] Y. Lee, D. Tran, K. Myhro, J. Velasco, N. Gillgren, C. N. Lau, Y. Barlas, J. M. Poirier, D. Smirnov, and F. Guinea, Competition between spontaneous symmetry breaking and single-particle gaps in trilayer graphene, *Nature Comm.* **5**, 5656 (2014).
  - [16] B. Pamuk, J. Baima, F. Mauri, and M. Calandra, Magnetic gap opening in rhombohedral-stacked multilayer graphene from first principles, *Phys. Rev. B* **95**, 075422 (2017).
  - [17] G. Chen, L. Jiang, S. Wu, B. Lyu, H. Li, B. L. Chittari, K. Watanabe, T. Taniguchi, Z. Shi, J. Jung, Y. Zhang,

- and F. Wang, Evidence of a gate-tunable mott insulator in a trilayer graphene moiré superlattice, *Nature Phys.* **15**, 237 (2019).
- [18] Y. Lee, S. Che, J. Velasco Jr., D. Tran, J. Baima, F. Mauri, M. Calandra, M. Bockrath, and C. N. Lau, Gate tunable magnetism and giant magnetoresistance in *abc*-stacked few-layer graphene, (2019), [1911.04450](#).
- [19] L.-J. Yin, L.-J. Shi, S.-Y. Li, Y. Zhang, Z.-H. Guo, and L. He, High-magnetic-field tunneling spectra of *abc*-stacked trilayer graphene on graphite, *Phys. Rev. Lett.* **122**, 146802 (2019).
- [20] B. L. Chittari, G. Chen, Y. Zhang, F. Wang, and J. Jung, Gate-tunable topological flat bands in trilayer graphene boron-nitride moiré superlattices, *Phys. Rev. Lett.* **122**, 016401 (2019).
- [21] G. Chen, A. L. Sharpe, P. Gallagher, I. T. Rosen, E. J. Fox, L. Jiang, B. Lyu, H. Li, K. Watanabe, T. Taniguchi, J. Jung, Z. Shi, D. Goldhaber-Gordon, Y. Zhang, and F. Wang, Signatures of tunable superconductivity in a trilayer graphene moiré superlattice, *Nature* **572**, 215 (2019), [arXiv:1901.04621](#).
- [22] G. Chen, A. L. Sharpe, E. J. Fox, Y.-H. Y. Zhang, S. Wang, L. Jiang, B. Lyu, H. Li, K. Watanabe, T. Taniguchi, Z. Shi, T. Senthil, D. Goldhaber-Gordon, Y.-H. Y. Zhang, and F. Wang, Tunable Correlated Chern Insulator and Ferromagnetism in Trilayer Graphene/Boron Nitride Moiré Superlattice, *Nature* **579**, 56 (2019), [1905.06535](#).
- [23] Y. Shi, S. Xu, Y. Yang, S. Slizovskiy, S. V. Morozov, S.-K. Son, S. Ozdemir, C. Mullan, J. Barrier, J. Yin, A. I. Berdyugin, B. A. Piot, T. Taniguchi, K. Watanabe, V. I. Fal'ko, K. S. Novoselov, A. K. Geim, and A. Mishchenko, Electronic phase separation in multilayer rhombohedral graphite, *Nature* **584**, 210 (2020).
- [24] H. Zhou, T. Xie, A. Ghazaryan, T. Holder, J. R. Ehrets, E. M. Spanton, T. Taniguchi, K. Watanabe, E. Berg, M. Serbyn, and A. F. Young, Half and quarter metals in rhombohedral trilayer graphene, *arXiv e-prints*, [arXiv:2104.00653](#) (2021), [arXiv:2104.00653 \[cond-mat.mes-hall\]](#).
- [25] N. P. Armitage, E. J. Mele, and A. Vishwanath, Weyl and dirac semimetals in three-dimensional solids, *Rev. Mod. Phys.* **90**, 015001 (2018).
- [26] Y. Cao, V. Fatemi, A. Demir, S. Fang, S. L. Tomarken, J. Y. Luo, J. D. Sanchez-Yamagishi, K. Watanabe, T. Taniguchi, E. Kaxiras, R. C. Ashoori, and P. Jarillo-Herrero, Correlated insulator behaviour at half-filling in magic-angle graphene superlattices, *Nature* **556**, 80 (2018), [arXiv:1802.00553](#).
- [27] Y. Cao, V. Fatemi, S. Fang, K. Watanabe, T. Taniguchi, E. Kaxiras, and P. Jarillo-Herrero, Unconventional superconductivity in magic-angle graphene superlattices, *Nature* **556**, 43 (2018).
- [28] W. Kohn and J. M. Luttinger, New mechanism for superconductivity, *Phys. Rev. Lett.* **15**, 524 (1965).
- [29] T. Cea and F. Guinea, Coulomb interaction, phonons, and superconductivity in twisted bilayer graphene, *Proceedings of the National Academy of Sciences* **118**, [10.1073/pnas.2107874118](#) (2021).
- [30] V. Tien Phong, P. A. Pantaleón, T. Cea, and F. Guinea, Band Structure and Superconductivity in Twisted Trilayer Graphene, *arXiv e-prints*, [arXiv:2106.15573](#) (2021), [arXiv:2106.15573 \[cond-mat.mes-hall\]](#).
- [31] F. Zhang, B. Sahu, H. Min, and A. H. MacDonald, Band structure of *abc*-stacked graphene trilayers, *Phys. Rev. B* **82**, 035409 (2010).
- [32] A. A. Zibrov, P. Rao, C. Kometter, E. M. Spanton, J. I. A. Li, C. R. Dean, T. Taniguchi, K. Watanabe, M. Serbyn, and A. F. Young, Emergent dirac gullies and gully-symmetry-breaking quantum hall states in *aba* trilayer graphene, *Phys. Rev. Lett.* **121**, 167601 (2018).
- [33] Y. Shi, S. Xu, Y. Yang, S. Slizovskiy, S. V. Morozov, S.-K. Son, S. Ozdemir, C. Mullan, J. Barrier, J. Yin, A. I. Berdyugin, B. A. Piot, T. Taniguchi, K. Watanabe, V. I. Fal'ko, K. S. Novoselov, A. K. Geim, and A. Mishchenko, Electronic phase separation in multilayer rhombohedral graphite, *Nature* **584**, 210 (2020).
- [34] T. O. Wehling, E. Şaşıoğlu, C. Friedrich, A. I. Lichtenstein, M. I. Katsnelson, and S. Blügel, Strength of effective coulomb interactions in graphene and graphite, *Phys. Rev. Lett.* **106**, 236805 (2011).
- [35] Note that we consider solely the Coulomb interaction associated to fluctuations of the total charge. The inclusion of a spin-dependent, inter-valley Hund coupling can allow for the existence of singlet solutions[5, 6].

*Supplementary Information for*  
**Superconductivity from Repulsive Interactions in Rhombohedral Trilayer  
 Graphene: a Kohn-Luttinger-Like Mechanism**

Tommaso Cea, Pierre A. Pantaleón, Võ Tién Phong and Francisco Guinea

In the main text, all numerical calculations are performed using a full six-band tight-binding model (TB). This captures accurately the evolution of the Fermi surface and associated van Hove singularities under the application of a perpendicular bias. However, this approach is numerically expensive because it requires Bloch wavefunctions throughout the entire Brillouin zone. Knowing that the low-energy physics is dominated by only wavefunctions near the zone corners. It is often useful to project to just these regions in momentum space to obtain a continuum model. Here, we characterize the small differences between the TB model and its various continuum models. From the Hamiltonian in Eq. (1) and following the procedure in Ref. [31], the low-energy Hamiltonian in valley  $\xi$  is given by

$$H = H_0 + H_s + H_{s'} + H_t + H_\Delta \quad (\text{S1})$$

where

$$\begin{aligned} H_0 &= \frac{v_0^3}{\gamma_1^2} \begin{pmatrix} 0 & (\pi^*)^3 \\ \pi^3 & 0 \end{pmatrix}, \\ H_s &= \left( \delta - \frac{2v_0v_4\mathbf{k}^2}{\gamma_1} \right) \sigma_0, \\ H_{s'} &= \Delta_2 \left[ 1 - 3 \left( \frac{v_0\mathbf{k}}{\gamma_1} \right)^2 \right] \sigma_0, \\ H_t &= \left( \frac{\gamma_2}{2} - \frac{2v_0v_3\mathbf{k}^2}{\gamma_1} \right) \sigma_x, \\ H_\Delta &= \Delta_1 \left[ 1 - \left( \frac{v_0\mathbf{k}}{\gamma_1} \right)^2 \right] \sigma_z, \end{aligned} \quad (\text{S2})$$

with  $\pi = \xi k_x + ik_y$ ,  $v_i = \frac{\sqrt{3}a\gamma_i}{2\hbar^2}$ ,  $a = 2.46 \text{ \AA}$ , and  $\mathbf{k} = \sqrt{k_x^2 + k_y^2}$ . The first term,  $H_0$ , is the simplest *ABC* trilayer Hamiltonian with only nearest-neighbour interlayer hopping and dominates at larger values of momentum  $\mathbf{k}$ . The second  $H_s$  term results from the weak coupling between the first and the third layer. The term  $H_{s'}$  is non-zero if the potential of the middle layer deviates from the average potential in layers 1 and 3. The term  $H_t$  is responsible for the trigonal warping in the band structure. The last term  $H_\Delta$  takes into account the external electrostatic potential acting at the outermost layers. This term breaks inversion symmetry and opens a gap that is responsible of the flattening of the bands.

In Fig. S1, we compare the full TB model in Eq. (1) with the continuum model in Eq. (S1) for different choices of parameters. In Fig S1(a), all parameters are non-zero, in this situation, as  $\Delta_1$  increases, we distinguish in the energy spectra a parabolic-like dispersion almost centered at  $K'$  point and two maxima. In the considered path, the maximum to the right corresponds to the Van Hove singularity in Fig. 5 of the main text. In Fig S1(b), we set to zero all the remote interlayer parameters except  $\gamma_0$ ,  $\gamma_1$  and  $\Delta_1$ . We find that the main features are preserved. However, in this case, we expect an increase in the DOS because both maxima are at the same energy. In Fig S1(c), we use the same conditions as in Fig S1(b), but we also remove the quadratic contribution in the last term in Eq. (S1), resulting in a term of the form  $H_\Delta = \Delta_1\sigma_z$ . As a function of  $\Delta_1$ , the bands near the Dirac point are always flat. If the filling is modified, there is no Lifshitz transition in the band structure. Figure S2 displays a density plot with the evolution of the valence bands for different values of the external displacement field  $\Delta_1$  in the full tight-binding model. The gray lines in each figure are the the isoenergy contours.

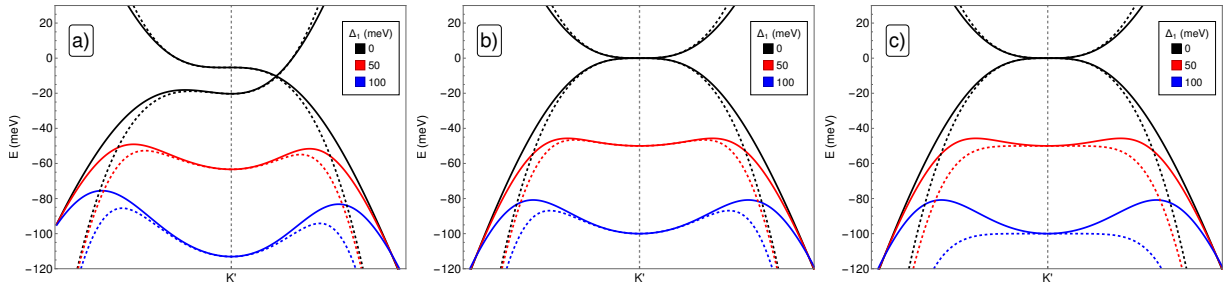


Figure S1. **Comparison of tight-binding and continuum models.** Band structure of ABC trilayer graphene for different values  $\Delta_1$ . Continuous lines are bands from the six-band full tight binding model of Eq. (1), and dashed lines the continuum low-energy bands of Eq. (S1) for different hopping values. In (a), all parameters are non-zero (as in Table 1 of the main text), in (b)  $\gamma_0, \gamma_1$  and  $\Delta_1$  are non-zero, and (c) is similar to (b) but without the quadratic term in  $H_\Delta$ .

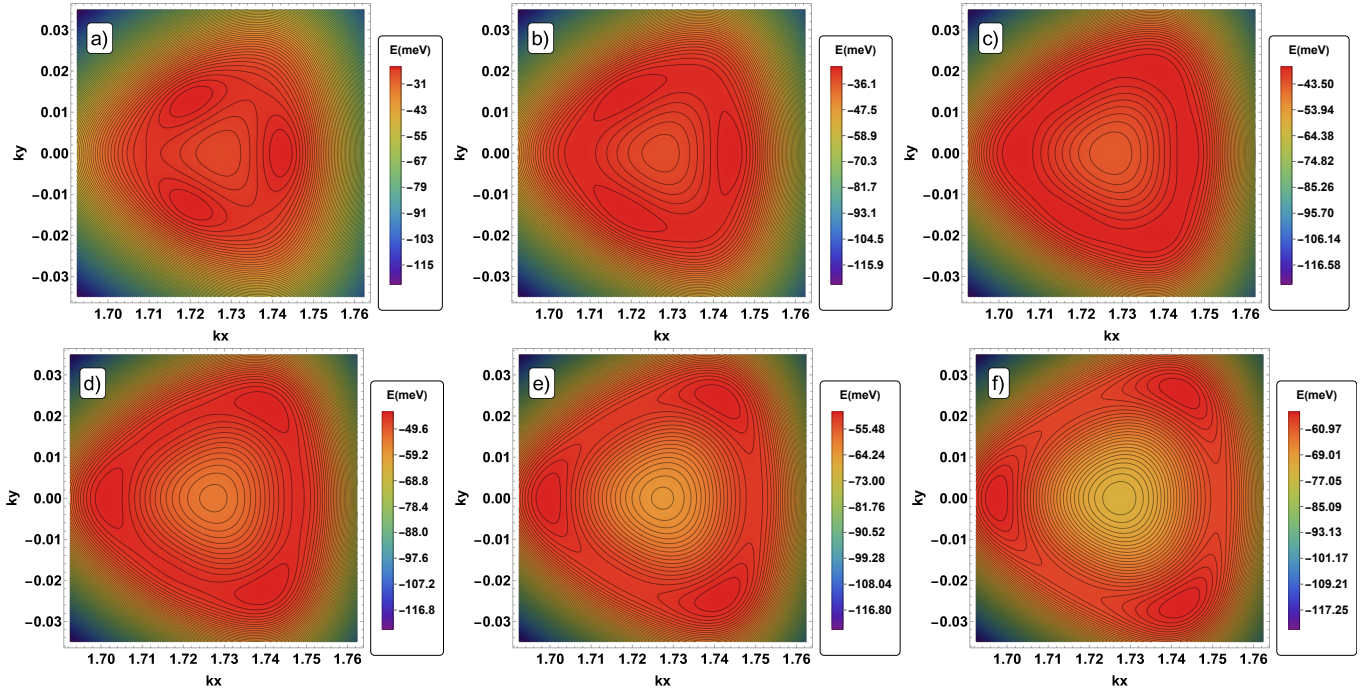


Figure S2. **Evolution of the valence band structure near the  $K'$  point.** Going from (a) to (f), the interlayer bias is increased as  $\Delta_1 = 10, 20, 30, 40, 50$  and  $60$  meV respectively. Here, we use the full tight-binding model.